Photobiogeochemical cycling of carbon monoxide in the southeastern Beaufort Sea in spring and autumn

Huixiang Xie[1]
Institut des sciences de la mer de Rimouski, Université du Québec à Rimouski, Rimouski, Québec G5L 3A1, Canada

Simon Bélanger
Département de biologie, chimie et géographie, Université du Québec à Rimouski, Rimouski, Québec G5L 3A1, Canada

Serge Demers
Institut des sciences de la mer de Rimouski, Université du Québec à Rimouski, Rimouski, Québec G5L 3A1, Canada

Warwick F. Vincent
Département de Biologie & Centre d'Études Nordiques, Université Laval, Québec City, Québec G1V 0A6, Canada

Tim N. Papakyriakou
Centre for Earth Observation Science, Department of Environment and Geography, University of Manitoba, Winnipeg, Manitoba R3T 2N2, Canada

Abstract

We investigated the distribution, photoproduction, microbial uptake, and air–sea exchange of carbon monoxide (CO), a key photoproduct of chromophoric dissolved organic matter (CDOM), in open waters of the southeastern Beaufort Sea in autumn 2003 and spring 2004. Diurnal cycles of surface water CO concentration ([CO]) occurred in autumn but not in spring. In both seasons [CO] was well above air-equilibrium at most stations (maximum of 12,500% saturation) and dropped with depth to undetectable levels below 50 m. Mean surface water [CO] and CO water-column burdens (0–50 m) were 0.45 nmol L^{-1} and 5.0 μmol m^{-2} in autumn and 4.7 nmol L^{-1} and 64.8 μmol m^{-2} in spring, and the sea-to-air CO flux was 33 times higher in spring. The efficiency of CO photoproduction correlated linearly with CDOM across the Mackenzie River estuary, the Mackenzie Shelf, and the Amundsen Gulf. Modeled water-column CO photoproduction in spring was 15 times that in autumn (45.8 vs. 3.0 μmol m^{-2} d^{-1}). Microbial CO uptake followed first-order kinetics in autumn while Hill-type, saturation, and inhibition kinetics were common in surface waters in spring. Bio-oxidation was the dominant CO loss term in autumn while gas exchange was almost equally important in spring. Higher photoproduction and slower bio-uptake in spring resulted in the wide autumn–spring differences in the [CO] distribution pattern and air–sea CO flux. CO cycling in cold northern waters differs both quantitatively and qualitatively from that in warmer seas.

Carbon monoxide (CO) is the dominant sink for hydroxyl radicals in the troposphere, thus affecting the lifetimes of greenhouse gases such as methane (Thompson

1992). The ocean has long been recognized as a source of atmospheric CO (Swinnerton et al. 1970; Bates et al. 1995; Stubbins et al. 2006a), albeit with large uncertainties in its source strength. Estimates of global open-ocean CO photoproduction also span an enormous range (30–820 Tg CO-C yr^{-1}), with recent studies giving lower values (30–90 Tg CO-C yr^{-1}; Zafiriou et al. 2003; Stubbins et al. 2006b). Photoproduction and microbial uptake are the primary source and sink for oceanic CO (Conrad et al. 1982), and the interplay between these processes results in large diurnal variations in CO concentration ([CO]) in the upper ocean (Conrad et al. 1982; Bates et al. 1995; Zafiriou et al. 2008).

CO is the second most abundant inorganic carbon product (after dissolved inorganic carbon [DIC]) resulting from the photodecomposition of chromophoric dissolved organic matter (CDOM) in marine waters, and it is thereby a significant component of the oceanic carbon cycle (Mopper and Kieber 2000). CO has been suggested as a proxy for the photoproduction of DIC (Miller and

Zepp 1995; Mopper and Kieber 2000) and biolabile organic carbon (Miller et al. 2002) and is a short-lived photoproduct that provides a useful tracer for modeling couplings among optics, photochemistry, biology, mixing dynamics, and gas exchange (Doney et al. 1995). The evaluation of CO photoproduction on global ocean scales is hindered by lack of data for coastal and estuarine areas and by inadequate accounting for the effects of CDOM quality and water temperature (Zhang et al. 2006).

Microbial CO oxidation is not only the main sink ($\sim 86\%$) of oceanic CO (Zafiriou et al. 2003), thus modulating its sea–air flux, but also potentially influences the flow of organic carbon in the food web and the respiratory CO_2 budget by providing supplemental energy to CO-oxidizing organisms (Moran and Miller 2007). Microbial CO uptake roughly follows first-order kinetics at ambient seawater concentrations (Zafiriou et al. 2003; Xie et al. 2005). Its rate constant (k_{bio}) co-varies with biological indicators such as chlorophyll *a* (Chl *a*; Xie et al. 2005) and bacterial cell abundance (H. Xie unpubl.) and recently its half-saturation concentrations (K_m: 1–18 nmol CO L^{-1}) have been found to be unexpectedly low (Tolli and Taylor 2005; Xie et al. 2005). CO oxidation is effected by a remarkable diversity of CO-oxidizing marine bacteria (Tolli et al. 2006; King and Weber 2007). While the genome-sequencing of the CO-oxidizer *Silicibacter pomeroyi* (Moran et al. 2004) has provided new insights into this process at the molecular and ecological levels, the species-level identities of other CO oxidizers remain elusive. Ecologically, the role of microbial CO oxidation in regulating the fate of marine organic carbon (Moran and Miller 2007) and CO air–sea exchange needs clarification, and more studies are required to quantify regional and global microbial CO loss.

Although the perennially low temperatures of the Arctic Ocean and its major inputs of terrigenous CDOM from large rivers (Retamal et al. 2007) present excellent opportunities to examine how extreme environments and climate change affect the photobiogeochemical behavior of CO, there are few reported concentration measurements (Linnenbom et al. 1973; Bates et al. 1995) and no investigations that include CO process studies. Highly variable factors in the Arctic include permanent and seasonal ice cover, extremes of solar radiation, and high influxes of freshwater and terrestrial dissolved organic matter (DOM; Opsahl et al. 1999). Global warming effects are predicted to occur earlier and more intensely at high northern latitudes than elsewhere (Flato et al. 2000), and may have already resulted in warmed surface waters, reduced extent, thickness, and duration of sea ice, and increased inputs of freshwater and terrestrial DOM (Frey and Smith 2005). Photochemistry, air–sea gas exchange, and microbial processes are all strongly influenced by these variables, and hence are sensitive to global warming. Contracting sea-ice cover, combined with increasing solar ultraviolet (UV) radiation over the high northern hemisphere (Fioletov et al. 2004), will permit more solar radiation to enter the water column, enhancing aquatic photoprocesses that affect the transformation and fate of terrestrial DOM (Opsahl and Benner 1998; Bélanger et al.

2006). Shrinking sea-ice cover should also accelerate air–seawater gas exchange, since sea ice serves as a barrier for this process, and rising temperatures and increased supply of organic substrates are expected to stimulate bacterial production.

Here we report the first study of the CO cycling in an Arctic marine ecosystem. Our purpose is to assess the seasonal variability of CO cycling in the Arctic Ocean and to evaluate whether this cycling (CDOM photochemistry, air–sea gas exchange, and microbiology) differs qualitatively and quantitatively from that in lower-latitude marine waters. Results from this study will also aid in refining estimates of regional and global oceanic CO production and loss fluxes.

Methods

Study areas—Fieldwork was within the Canadian Arctic Shelf Exchange Study (CASES) and occurred during the open water cruises of the *CCGS Amundsen* in the southeastern Beaufort Sea (Fig. 1), in autumn from 26 September to 15 October 2003 (CASES leg 1), and in spring from 03 June to 22 June 2004 (CASES leg 7). These cruises took place over the Mackenzie Shelf (MS) and Amundsen Gulf (AG) with some stations (Sta.; CA7 and CA11–CA14) in the Canada Basin. The MS and AG were ice-free in autumn until freezing began in parts of the AG late in the cruise. The spring cruise was restricted to the Cape Bathurst polynya in the AG because of high ice cover on the MS. Stations (R4, R5a, R5d, and R9) in the Mackenzie River estuary were occupied in late July and early August 2004 during the Arctic River-Delta Experiment (ARDEX) aboard *CCGS Nahidik* and were sampled for determinations of apparent quantum yield (AQY) for CO photoproduction (Φ_{co}; *see* below).

The major freshwater source to the region is the Mackenzie River, the only North American analogue to the large Siberian rivers flowing into the Arctic. Its freshwater discharge (249–333 km^3 yr^{-1}) and DOC export (1.3 Tg yr^{-1}) are the fourth-highest among the large Arctic rivers, but it exhibits the largest particulate organic carbon delivery (1.8–2.1 Tg yr^{-1}; Dittmar and Kattner 2003). The discharge of riverine particulate matter is mainly restricted to the MS (200 km wide); however, the DOM-laden river plume extends across the shelf, influencing the interior ocean under easterly winds. Otherwise, the river plume tends to bend eastward, flowing along the Tuktoyaktuk Peninsula toward the AG (Carmack and Macdonald 2002). The high and low flow periods of the Mackenzie River are in spring–summer and fall–winter, respectively, with the freshet usually occurring in May and 70% of the annual discharge delivered between May and September.

CO sampling and analysis—Samples were collected for determining surface water [CO] ($[CO]_{surf}$), CO profiles, microbial uptake kinetics, and Φ_{co} at locations and seasons as shown in Table 1. While the ship was stationed, surface water was sampled at intervals of 0.5–2 h by lowering a stainless steel bucket sideways through the surface to minimize turbulence. Custom-built titanium bottles (6-liter;
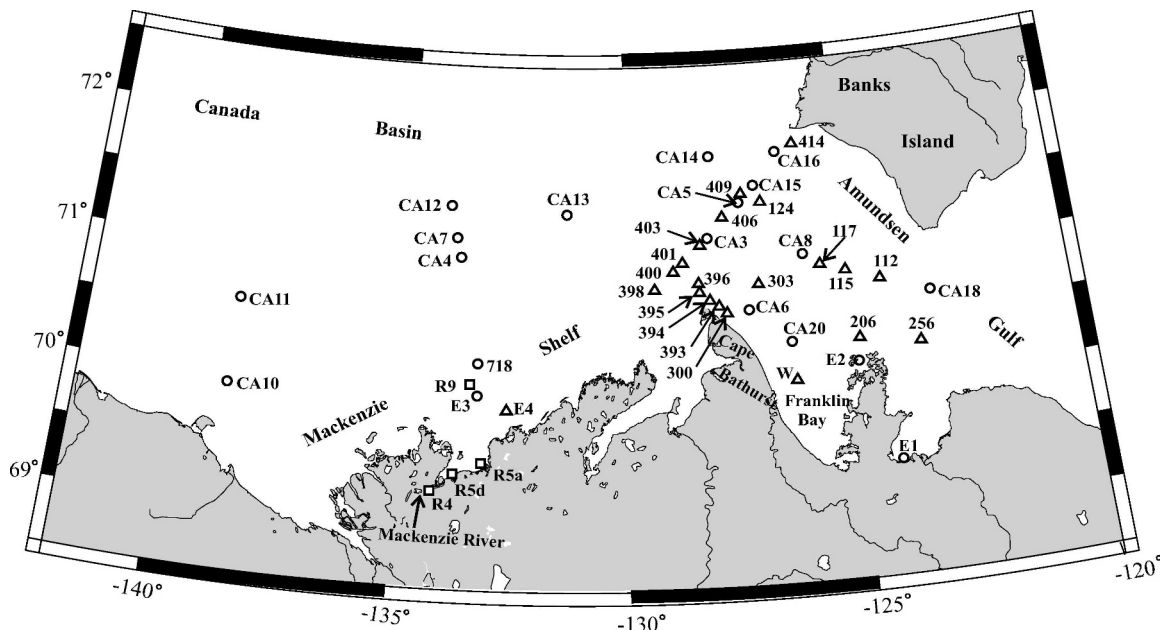
Fig. 1.   Study areas and sampling stations. Circles: stations sampled in September and October 2003 (CASES leg 1); triangles: stations sampled in June 2004 (CASES leg 7); squares: stations sampled in July 2004 (ARDEX). Sta. 409 and 718 were also sampled in July 2004 (CASES leg 8). Sta. CA18 and CA20 were also sampled in June 2004.

Doherty et al. 2003), were deployed on standard conductivity–temperature–depth (CTD) rosettes to collect profile samples. Immediately after samples arrived on deck, subsamples were drawn in a weatherproof shelter into 50-mL metal-tipped ground-glass syringes (Perfectum®) fitted with three-way nylon valves (Kontes®). They were rinsed with sample water three times, including ≥1 bubble-free flushing before the final drawing. Subsamples, taken in duplicate when possible, were warmed up to room temperature in the dark and analyzed within 1 h. Only one subsample per bottle was available during the latter half of the autumn cruise; however, the good reproducibility of replicates (3%; *see* below) suggests that this had little effect on quality of the CO profiles. The six titanium bottles have been shown to be free of CO contamination (Xie et al. 2002; Zafiriou et al. 2008) and were rechecked during the autumn cruise by lowering them to 300 m at Sta. CA15 and measuring [CO], yielding 0.027–0.038 nmol L^{-1} CO (mean: 0.033 nmol L^{-1}). This value is essentially identical to the syringe-plus-instrument blank (*see* below) and to the values for deep Sargasso Sea waters (Zafiriou et al. 2008). Niskin bottles (12-liter) for general-purpose sampling were also checked concurrently. Eighteen of 20 Niskin bottles gave a mean [CO] of 0.034 nmol L^{-1} (range: 0.025–0.047 nmol L^{-1}), but two showed higher values (~0.075 nmol L^{-1}). Hence, 90% of the Niskin bottles were as good as titanium ones for CO sampling, contrary to prior observations that plastic samplers are often fraught with erratic, hard-to-correct CO contamination (Xie et al. 2002). The low CO blanks of the CASES Niskin bottles are likely due to contamination-reducing measures, including Teflon-coated inside walls and silicon springs. The bottles were also kept in a weatherproof shelter, which eliminated exposure to solar

radiation except during CTD casts. Since sunlight exposure is probably the primary cause of CO contamination by plastics (Xie et al. 2002), use in a low-light environment probably ensured the Niskin bottles' acceptability, but low temperatures may also have lowered blanks, since CO photoproduction from organics is temperature-dependent (Zhang et al. 2006). To facilitate coordination of sampling with others, we used the "good" Niskin samplers.

[CO] was measured using a manual headspace method (Xie et al. 2002). Briefly, 5 mL CO-free air was introduced into the sample-filled syringes (1 : 7 gas : water ratio). The syringe was vigorously shaken for 3 min and the equilibrated headspace air was injected into a modified Reduction Gas Analyzer (RGA3; Trace Analytical) for CO quantification. The system was standardized by frequent injections of a gaseous CO standard (Praxair) using a wetted 10-mL glass syringe (100% relative humidity). The CO standard has a nominal concentration of 0.122 Pa; recalibration against a National Institute of Standards and Technology (NIST)-traceable 0.993 Pa standard gave 0.125 Pa, the valued used here (Zafiriou et al. 2008). An all-inclusive estimate of analytical variability for in situ samples was made at sea based on 299 duplicate measurements by three analysts. Average [CO] was 2.04 nmol L^{-1} (range: 0.015–9.24 nmol L^{-1}); the average difference in each pair was 0.061 nmol L^{-1}, or 3.0%. The instrument-plus-syringe blank based on analyzing seven replicates of sterilized seawater extensively bubbled with CO-free air was 0.030 ± 0.004 nmol L^{-1}. This blank was subtracted from all samples, resulting in a few slightly negative [CO] values that were reset to zero.

Air samples were drawn in duplicate at the bow, facing the wind, into internally water-wet 10-mL glass syringes at

Table 1. Latitude (Lat) and longitude (Long) of stations (Sta.) sampled for measurements of $[CO]_{surf}$, [CO] depth profiles, k_{bio}, and Φ_{co}. Key: AU = autumn, SP = spring, SU = summer.

Designation		Position		Measured parameters			
Sta.	Season	Lat, °N	Long, °E	$[CO]_{surf}$	CO	k_{bio}	Φ_{co}
112	SP	70.756	−124.260	x	x		
115	SP	70.852	−125.032	x	x		
117	SP	70.912	−125.579	x	x	x	x
124	SP	71.422	−126.861	x	x		
206	SP	70.321	−124.842	x	x	x	
256	SP	70.252	−123.503	x	x		
300	SP	70.584	−127.758	x	x		
303	SP	70.795	−127.000	x	x		
393	SP	70.634	−127.922	x			
394	SP	70.692	−128.140	x			
395	SP	70.751	−128.323	x			
396	SP	70.809	−128.362	x			
398	SP	70.791	−129.359	x	x		
400	SP	70.917	−128.914	x	x	x	
401	SP	70.982	−128.714	x			
403	SP	71.120	−128.307	x	x		
406	SP	71.331	−127.736	x	x	x	
409	SP	71.494	−127.304	x	x		
409	SU	71.494	−127.304				x
414	SP	71.849	−125.989	x	x		x
718	AU	70.210	−133.309	x	x	x	
718	SU	70.210	−133.309				x
CA3	AU	71.165	−128.103	x	x		
CA4	AU	71.023	−133.776	x		x	
CA5	AU	71.430	−127.350	x	x	x	
CA6	AU	70.597	−127.243	x	x	x	
CA7	AU	71.168	−133.889	x		x	
CA8	AU	71.000	−125.965	x	x		
CA10	AU	69.929	−138.737	x	x	x	
CA11	AU	70.575	−138.669	x			
CA12	AU	71.410	−134.065	x	x		
CA13	AU	71.360	−131.370	x		x	
CA14	AU	71.788	−128.008	x	x	x	
CA15	AU	71.546	−126.996	x	x		
CA16	AU	71.797	−126.416	x	x	x	
CA18	AU	70.631	−123.115	x	x		
CA18	SP	70.631	−123.115			x	x
CA20	AU	70.336	−126.345	x	x		
CA20	SP	70.336	−126.345	x	x		
E1	AU	69.374	−124.215	x			
E2	AU	70.151	−124.920	x		x	
E3	AU	69.968	−133.303	x		x	
E4	SP	69.863	−132.646				x
R4	SU	69.227	−134.227				x
R5a	SU	69.456	−133.147				x
R5d	SU	69.362	−133.740				x
R9	SU	70.050	−133.417				x
W	SP	70.046	−126.301				x

intervals of 0.5–2 h and analyzed for CO concentration ($[CO]_{atm}$) within minutes by direct injection into the RGA3 loop in the same manner as the gas standard.

Determination of Φ_{co}—Φ_{co} spectra were determined using samples from selected stations, including Sta. 409 and 718, which were sampled in July 2004 on CASES leg 8 (Table 1). During the CASES cruises, water (~2–5 m deep) was sampled in Niskin bottles, while at Sta. E4 a helicopter-deployed high-density polyethylene bucket was used. Samples were gravity-filtered upon collection through a Pall AcroPak 1000 Capsule sequentially containing 0.8- and 0.2-μm polyethersulfone membranes. During the ARDEX cruise, surface water was collected using a plastic bucket and transferred to carboys. The bucket and carboys were acid-cleaned and rinsed profusely with sample water prior to sampling. The water was then filtered sequentially through 3- and 0.2-μm polysulfone filters. Filtration and

Xie et al.

Table 2. Fitted parameters for Eq. 1 and other related variables. Key: SP = spring, SU = summer.

Sta.	Season	Salinity	Incubation T (°C)	a_{330} (m^{-1})	a_{412} (m^{-1})	$m_1 \times 10^{11}$	m_2	m_3	$\overline{\Phi}_{co} \times 10^{6}$*
W	SP	30.76	−0.5	0.85	0.23	3.66	4818.7	43.96	1.11
E4	SP	0.97	−0.5	12.30	2.94	1010	2650.8	−11.90	5.05
CA18	SP	30.09	−0.5	0.71	0.17	3.30	5046.6	56.35	1.21
117	SP	30.61	−0.5	0.64	0.15	3.27	5089.2	57.64	1.28
414	SP	30.47	−0.5	0.35	0.08	1.89	5452	70.46	1.18
R4	SU	0.13	18.0	5.79	1.26	9000	1233.5	−123.79	4.59(2.85)
R5a	SU	8.19	12.0	4.71	1.02	4600	1436.5	−106.53	3.55(2.56)
R5d	SU	1.57	13.0	5.27	1.13	7780	1215.4	−126.29	3.88(2.72)
R9	SU	25.81	9.0	1.52	0.33	328	2509.7	−46.31	2.24(1.94)
409	SU	28.79	−0.5	0.59	0.13	2.86	5205.4	64.44	1.21
718	SU	25.40	−0.5	1.24	0.28	35.6	3599.6	−0.93	1.69

* Numbers in parentheses are $\overline{\Phi}_{co}$ values after correction to T = −0.5°C using the $\overline{\Phi}_{co}$–T relationships in Zhang et al. (2006). Based on a_{330}, the $\overline{\Phi}_{co}$–T relationship for Sta. 3 in Zhang et al. (2006) was used for Sta. R4, R5a, and R5d in the present study, and the relationship for Sta. 11 in that study was used for Sta. R9 here.

sample transfer were conducted under dim room light. Filtered samples were stored at 4°C in the dark in acid-cleaned clear glass bottles (4-liter), shipped to the laboratory at Rimouski, and refiltered with 0.2-μm polyethersulfone membranes immediately prior to absorbance measurements and irradiations, carried out within 2 months of sampling. Absorbance spectra were recorded from 200 nm to 800 nm at 1-nm increments with a PerkinElmer lambda-35 dual-beam spectrometer fitted with 10-cm rectangular quartz cells, referenced to Nanopure water. Baselines were corrected by subtracting the absorbance averaged over 683–688 nm from all absorbance values (Babin et al. 2003). Absorption coefficients (a, m^{-1}) were calculated as 2.303 times the absorbance divided by the light path. The lower detection limit was 0.03 m^{-1}, permitting measurement of a up to ~580 nm (median a_{580}: 0.058 m^{-1}; range: 0.031–0.36 m^{-1}). CDOM absorption coefficients at 330 nm and 412 nm (a_{330} and a_{412}) are provided in Table 2.

The setup and procedure for determining Φ_{co} spectra were described by Zhang et al. (2006). Briefly, water samples were purged with CO-free air, transferred into precombusted (420°C) gas-tight quartz-windowed cylindrical cells (104 mL), and irradiated at their in situ temperatures (±1°C; Table 2) using a SUNTEST CPS solar simulator equipped with a 1-kW xenon lamp. Eight spectral treatments employed successive Schott long band-pass glass filters: WG280, WG295, WG305, WG320, WG345, GG395, GG435, and GG495. Spectral irradiance under each filter was measured using an OL-754 spectroradiometer fitted with a 2-inch (5.08 cm) OL IS-270 integrating sphere calibrated with an OL 752-10E irradiance standard. Irradiation times (0.28–4 h) were adjusted to ensure that considerable amounts of CO were produced but minimum absorbance losses occurred.

The CO apparent quantum yield at wavelength λ, $\Phi_{co,\lambda}$, was defined as the number of mol of CO produced per mol of photons absorbed by CDOM at that wavelength. The number of photons absorbed by CDOM at wavelength λ, $Q_{a\lambda}$, is (Hu et al. 2002) $Q_{0,\lambda} \times (a_{cdom,\lambda} / a_{t,\lambda}) \times A \times [1 - \exp(-a_{t,\lambda} \times L)]$ (mol photons s^{-1} nm^{-1}), where A is the

cross-section and L the path-length of the irradiation cells, $Q_{0,\lambda}$ is the photon flux just below the front window, and $a_{t,\lambda}$ is the total absorption coefficient, the sum of the absorption by CDOM ($a_{cdom,\lambda}$) and water ($a_{w,\lambda}$). Values of $a_{w,\lambda}$ were taken from Pope and Fry (1997) and Buiteveld et al. (1994). Iterative curve-fitting of parameters m_1, m_2, and m_3 to Eq. 1 was employed to derive Φ_{co} spectra,

$$\Phi_{co,\lambda} = m_1 \times \exp\left(\frac{m_2}{\lambda + m_3}\right) \tag{1}$$

This treatment is modified from Johannessen and Miller (2001; Bélanger et al. 2006; Zhang et al. 2006). CO production rates predicted from the retrieved Φ_{co} spectra agreed well with measured rates, with R^2 ranging from 0.988 to 1.000 ($n = 11$). A direct intercomparison by Ziolkowski and Miller (2007) also confirmed that this approach agrees with the traditional monochromatic method for retrieving Φ_{co} spectra.

To facilitate analyzing Φ_{co} variability, we defined a regionally suitable solar spectrum-weighted mean quantum yield, $\overline{\Phi}_{co}$, over λ 280–600 nm (Bélanger et al. 2006; Zhang et al. 2006),

$$\overline{\Phi}_{co} = \frac{\int\limits_{280}^{600} Q_\lambda \Phi_{co,\lambda} d\lambda}{\int\limits_{280}^{600} Q_\lambda d\lambda} \tag{2}$$

Q_λ is the surface-spectral solar photon fluxes at 70°N, 133°W at 14:00 local time (LT) on 01 July (*see* Web Appendix 1: www.aslo.org/lo/toc/vol_54/issue_1/0234a1.pdf), simulated using the model of Gueymard (2001) under cloudless conditions with an ozone column burden of 330 Dobson Units. The $\overline{\Phi}_{co}$ values are specific to these conditions.

Kinetic study of microbial CO consumption—First-order rate constants of microbial CO consumption (k_{bio}) were determined according to Xie et al. (2005). Water from Niskin bottles or a hand-held polyethylene bucket was drawn while protected from light into acid-cleaned 200-mL

all-glass syringes fitted with three-way plastic valves. The syringes were incubated in the dark at the samples' in situ temperatures ($\pm 0.5°C$) and analyzed for [CO] at appropriate times (usually four to five points per series). Each time series was fitted by an exponential, yielding k_{bio}. This method measures net-loss rate constants at [CO] slightly below initial [CO]. These net-loss rate constants should be close to the corresponding gross-loss rate constants, since thermal CO production, determined on cyanide-poisoned samples, was negligible over the incubations. At high [CO], microbial uptake may deviate from first-order kinetics, requiring Wright–Hobbie kinetics (Tolli and Taylor 2005; Xie et al. 2005) to derive limiting rates, V_{max} and half-saturation substrate concentrations, K_m, that more accurately characterize the data. To determine V_{max} and K_m, triplicate incubation syringes were amended with CO-free or CO-enriched air, shaken for 3 min, the headspace gas expelled, yielding three different initial [CO]. Each syringe was analyzed close to the time of preparation, incubated in the dark, and analyzed sequentially three more times. Taking mean rates of CO consumption as differences between adjacent points, we plotted all the data for a given sample as nonlinear Wright–Hobbie kinetics. There was often a significant [CO] change between adjacent points; hence, the plotted rates are linear approximations.

Meteorology—Underway measurements of apparent horizontal wind speed and direction were made using a wind monitor (RM Young; 05103-MA) from an instrumented tower on the foredeck of the *CCGS Amundsen*. The nominal height of the monitor ranged from 15.50 m to 15.95 m above the sea surface. Wind speed and direction were scanned at 3-s intervals by a micrologger (Campbell Scientific 23X and CR1000) and archived on a personal computer as 1-min averages. True wind speed and direction were calculated following Smith et al. (1999). Ship speed and direction over ground were calculated based on the rate of change of the ship's location at 1-min intervals. Data corresponding to apparent wind directions of 120–240° (aft of the monitor) were removed. Wind speed was corrected to 10-m height using the National Oceanic and Atmospheric Administration's Coupled Ocean Atmosphere Response Experiment version 3.0 algorithm. Sea-surface temperature and salinity (≤ 5 m) were obtained from numerous CTD profiles (SeaBird SBE 911 plus) distributed across the CASES domain.

A GUV-510 radiometer (Biospherical Instruments) mounted atop the *Amundsen*'s wheelhouse recorded cosine-corrected down-welling irradiances of photosynthetic active radiation (PAR; 400–700 nm) and at five 10-nm channels centered at 305, 313, 320, 340, and 380 nm. The 2-s time-resolution data were smoothed to 10-min intervals by time-weighted averaging. Instrumental failure resulted in no surface irradiance data from day of the year (DOY) 269–271 and DOY 279–281. For these periods, surface down-welling irradiances at intervals of 10 min were estimated using the SBDART (Santa Barbara DISORT Atmospheric Radiative Transfer) software. The model's inputs include solar zenith angle, total ozone concentration, and cloud optical thickness. The latter two were derived

from satellite measurements distributed by ISCCP (International Satellite Cloud Climatology Project; http://isccp. giss.nasa.gov/). ISCCP data, provided on a 280-km equal-area grid every 3 h, were spatially interpolated. On days with in situ irradiance data, the model output displayed day-to-day patterns similar to the data, agreeing at 320 nm to within 23% ($\pm 14\%$, $n = 12$).

Gas exchange—Surface water [CO] in equilibrium with the atmosphere ($[CO]_{eq}$) were calculated using measured $[CO]_{atm}$ and Henry's law constants (Wiesenburg and Guinasso 1979). CO air–sea fluxes were assessed using the transfer velocity–wind-speed relationships of Wanninkhof (1992) and Liss and Merlivat (1986) with CO Schmidt numbers from Zafiriou et al. (2008). The Liss and Merlivat (1986) values are presumably more applicable to fetch-limited lake-type areas, while the former apply to fetch-unlimited oceanic environments (Wanninkhof 1992). Except at low winds (≤ 0.5 m s^{-1}), Wanninkhof's relationship gives about twice the transfer velocities of the Liss and Merlivat (1986) relationship. Since the open waters we visited are larger than ordinary lakes but may still be affected by wind fetch, we bracketed gas flux estimates assuming that the Liss and Merlivat (1986) relationship yields lower limits and the Wanninkhof relationship yields upper limits. Spot and monthly climatological wind speeds were used to calculate instantaneous and climatological (seasonal and regional) fluxes, respectively. The climatological winds were extracted from the Comprehensive Ocean–Atmosphere Data Set (1960–2005). Spot wind speeds were linearly interpolated to times of $[CO]_{surf}$ measurements. Instantaneous fluxes at time-series stations were time-weighted. Climatological fluxes were calculated for the MS and the AG separately: each was divided into 1° × 1° bands to match the climatological wind speed fields. $[CO]_{surf}$ was averaged over time-course measurements, when available. CO fluxes computed for individual stations were averaged over each 1° × 1° band, and these values were averaged to obtain regional fluxes. Sparse coverage and variable ice cover prevented making flux estimates for the Canada Basin.

Results

General meteorological, physical, and biological properties—Similar averages and ranges of wind speeds were observed in spring and autumn in the AG. In autumn, ranges and averages of wind speed for the AG and the MS were also comparable. Daily averaged E_{d320} in spring was 21 and 10 times that in autumn for the AG and entire study area (Table 3). Unsurprisingly, sea-surface temperature (SST) showed little spatial and spring–autumn ("seasonal" hereafter) variation. SST rose conspicuously with time during spring from $-0.95°C$ (Sta. 206) to $1.85°C$ (Sta. CA20), contributing to more scattered SST data then. Sea-surface salinity (SSS) exhibited relatively large spatial and seasonal variability. Seasonally, surface water in the AG was considerably fresher in autumn than in spring, despite the high (spring) vs. low (autumn) river flow cycle. Freshwater input from the Mackenzie River was largely

Table 3. Summary of seasonality of forcings and CO responses. Values are ranges and/or means ± standard deviation. Key: MS = Mackenzie Shelf, AG = Amundsen Gulf. Air–sea flux estimates are based on the Wanninkhof formulation.

Property	Autumn	Spring (AG only)
Forcings		
Sea-surface temperature ($^\circ$C)	Overall: -1.43–-0.11, -0.99 ± 0.37 AG: -1.11–-0.11, -0.77 ± 0.34	-1.24–1.85, 0.17 ± 1.14
Sea-surface salinity	Overall: 21.35–27.60, 25.62 ± 1.75 AG: 23.45–27.60, 25.92 ± 1.67	30.18–31.35, 30.65 ± 0.28
Wind speed (m s^{-1})	Overall: 0.12–17.9, 7.1 ± 3.9 AG: 0.12–13.2, 5.8 ± 3.2	0.10–16.5, 6.1 ± 3.0
Insolation at 320 nm (j m^{-2} d^{-1})	Overall: 210–886, 482 ± 240 AG: 210–261, 236 ± 19.0	3043–6855, 4944 ± 1281
Chl a (mg m^{-2})	Overall: 10.2–41.7, 19.8 ± 10.3 AG: 15.3–41.7, 25.6 ± 11.0	2.0–360.0, 86.5 ± 108.8
$a_{cdom,350}$ (m^{-1})	Overall: 0.27–1.25, 0.64 ± 0.30 AG: 0.27–1.25, 0.72 ± 0.34	0.31–0.53, 0.40 ± 0.066
Carbon monoxide		
$[CO]_{air}$ (10^{-3} Pa)	Overall: 7.05–11.4, 9.39 ± 0.99 AG: 9.24–11.4, 10.4 ± 0.46	7.28–9.46, 8.32 ± 0.37
$[CO]_{surf}$ (nmol L^{-1})	Overall: 0.12–1.52, 0.36 ± 0.25 AG: 0.17–1.34, 0.45 ± 0.34	0.98–13.0, 4.72 ± 2.42
Column burden (μmol m^{-2})	Overall: 1.45–10.7, 5.54 ± 2.38 AG: 1.45–7.13, 4.96 ± 1.69	25.6–136.6, 64.8 ± 31.7
Sea–air saturation factor	Overall: 0.94–13.4, 2.9 ± 2.1 AG: 1.3–10.3, 3.5 ± 2.7	9.4–125.1, 45.4 ± 23.4
Sea–air flux (μmol m^{-2} d^{-1})		
Spot wind speed	Overall: -0.047–1.47, 0.35 ± 0.32 AG: 0.010–1.47, 0.19 ± 0.31	0.059–44.3, 6.20 ± 6.43
Climatological wind speed	MS: 0.41; AG: 0.51	18.2
k_{bio} (d^{-1})	Overall: 0.26–1.39, 0.69 ± 0.33 AG: 0.26–0.74, 0.49 ± 0.22	0.10–0.43, 0.23 ± 0.13
$P_{co,0}$ (nmol L^{-1} d^{-1})	MS: 12.4; AG: 3.9	29.6
$P_{co,col}$ (μmol m^{-2} d^{-1})	MS: 3.8; AG: 3.0	45.8

retained inshore behind the sea-ice pressure ridge (stamu-khi) until late June (Galand et al. 2008), and oxygen isotopic analysis indicated that more river water was diverted into the AG in autumn (R. Macdonald unpubl.). Spatially, low SSS values (21.35–24.56) in autumn occurred near stronger fluvial influence: near the Mackenzie estuary (Sta. 718) and near the south shore of the AG (Sta. CA3, CA6, and CA20). Higher SSS values (25.46–27.60) characterized the remaining areas. SSS exhibited little spatial variability in the AG in spring, consistent with the lower river input to this region at that time.

Depth-integrated (0–100 m) Chl a concentration varied 180-fold in spring (Table 3), suggesting extreme patchiness in biomass and rapid spatiotemporal evolution of the spring bloom. In contrast, Chl a was far more uniform in autumn in the gulf and also in the entire area. In the gulf, mean Chl a in spring was 3.3 times that in autumn. In contrast, surface-water CDOM abundance (a_{350}), in the gulf exhibited a larger range and a higher average in autumn, in line with the idea above that the gulf was more strongly influenced by river runoff at that time.

[CO]$_{surf}$, [CO]$_{atm}$, and gas exchange—Mean $[CO]_{surf}$ in the AG was 10-fold higher in spring than in autumn (Table 3). In the gulf, spring also displayed a broader [CO] range (~13-fold) than autumn (~8-fold). The overall mean

and range of $[CO]_{surf}$ for the autumn cruise were similar to those for the gulf section. The highest $[CO]_{surf}$ in autumn all occurred in the Mackenzie River plume: Sta. 718 (1.53 nmol L^{-1}), CA3 (0.98 nmol L^{-1}), and CA6 (1.35 nmol L^{-1}). $[CO]_{surf}$ exhibited 2–3-fold diurnal variations at Sta. E1, E2, and 718, with peaking in late afternoon (18:00–19:00 LT; Fig. 2), ~2–4 h after peak insolation. $[CO]_{surf}$ at Sta. E2 was inversely related to wind speed; no other stations were occupied long enough to verify this feature. There were large spatiotemporal variations also in spring, with initially low $[CO]_{surf}$. Among the stations continually monitored (28–37 h each; Fig. 2 shows three of five instances), time-averaged $[CO]_{surf}$, in ascending order, was Sta. 206 (2.51) < Sta. 117 (3.22) < Sta. 303 (4.01) < Sta. CA18 (4.59) < Sta. 406 (8.39; parentheses indicate $[CO]_{surf}$ in nmol L^{-1}). $[CO]_{surf}$ showed larger time variations at Sta. CA18 and 117, 4.8- and 6.5-fold, vs. 2.1–2.5-fold elsewhere. Patterns of $[CO]_{surf}$ vs. time varied, but none revealed clear diurnal signals (Fig. 2).

The ranges and seasonal trend of $[CO]_{atm}$ (Table 3) agree with those reported by Novelli et al. (1998) for high northern latitudes. Surface water was supersaturated with CO relative to air except on rare occasions in autumn when it was slightly undersaturated. The saturation ratio, $[CO]_{surf}$ / $[CO]_{eq}$ (i.e., [CO] at equilibrium with air), spanned large ranges in both seasons (Table 3), but the
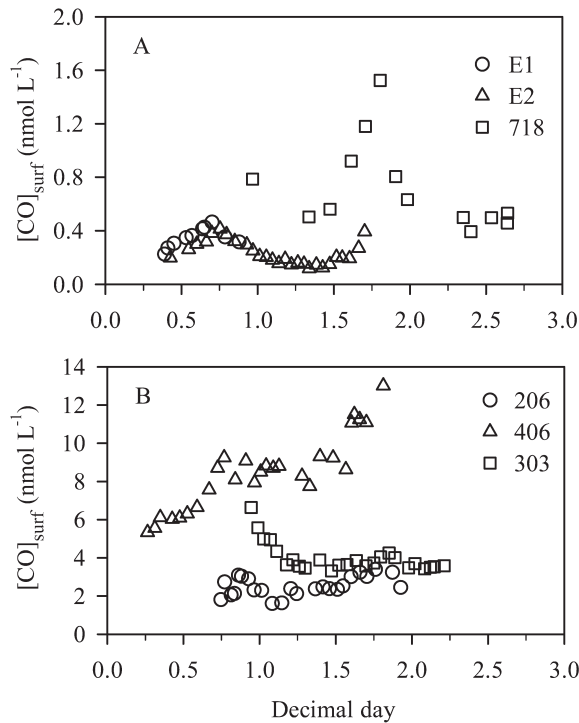
Fig. 2. [CO]$_{surf}$ at time-course stations in (A) autumn and (B) spring. Decimal day is referenced to the integral year day of the time-zero sample.
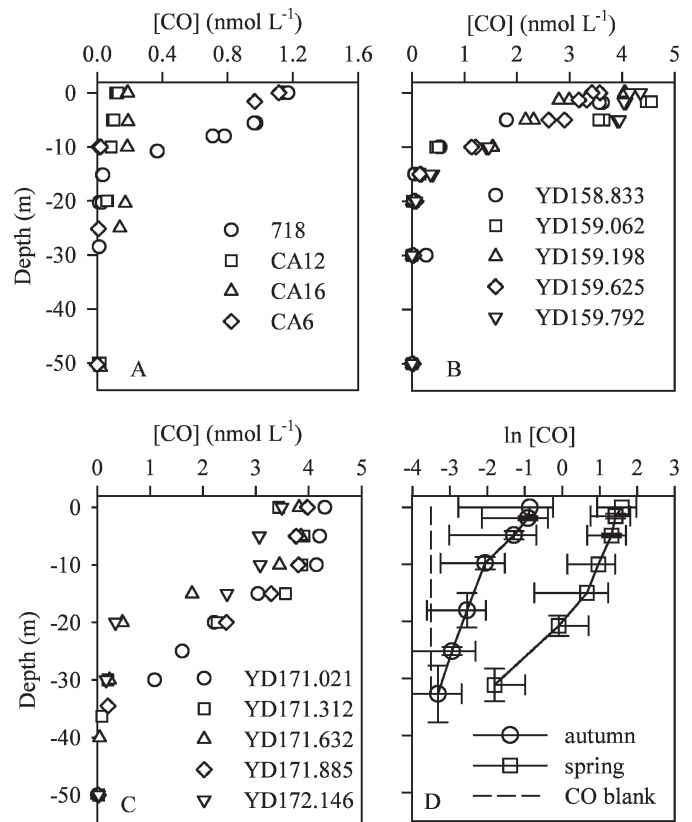

Fig. 3. Representative CO depth profiles in (A) autumn and (B, C) spring (Sta. CA18, Sta. 303), and (D) logarithmically scaled cruise mean CO profiles. Total 16 CO profiles acquired from 12 stations in autumn and 37 profiles from 14 stations in spring (*see* Table 1).

mean ratio for the gulf was 13 times higher in spring. This prevalent supersaturation led to net sea-to-air CO fluxes in both seasons, but in spring the flux was ~33–40 times larger, regardless of the formulation or wind field used to calculate transfer velocities. Climatological fluxes were more than twice the mean instantaneous fluxes, implying that our cruises were in unusually low-wind periods. As expected, fluxes based on the Wanninkhof relationship were roughly twice those based on the Liss and Merlivat (1986) relationship. To assess area-integrated CO fluxes, cruise-mean ice-free water areas were computed from daily sea-ice concentrations (data from the National Snow and Ice Data Center): 74.3×10^3 km^2 on the MS (autumn), 85.0×10^3 km^2 (autumn), and 38.2×10^3 km^2 (spring) in the AG. Based on wind climatology, mean daily fluxes during the cruises were 15.6–30.5 mol on the MS (autumn), 22.1–43.4 mol (autumn), and 351.4–695.2 mol (spring) in the AG. While yearly extrapolation is fraught with uncertainties, due primarily to the lack of summer [CO] data, we estimate that 43.1–84.8×10^3 and 50.4–99.7×10^3 mol of CO are emitted from the MS and AG, totaling 93.5–184.5×10^3 mol, by approximating that the mean of autumn and spring fluxes in the AG represents annual values and that the spring-to-autumn flux ratio on the MS is the same as in the AG, and then scaling to the means of the yearly averaged ice-free water areas in 2003 and 2004, 30.9×10^3 km^2 on the MS and 29.2×10^3 km^2 in the AG.

Depth distribution—An initial broad generalization was made by averaging all CO profiles for each season (Fig. 3D). [CO] was always negligible at ≥50 m and higher

in spring (~5–25-fold) than in autumn at <31 m, and both the spring and autumn profiles showed nearly exponential decreases in [CO] with depth, consistent with a photochemical source in the surface layer, a microbial sink throughout the water column, and incomplete vertical mixing. CO depth profiles from the time-series stations in spring did not exhibit diurnal signals at any depth (Fig. 3B,C). The role of vertical mixing in regulating CO depth distribution was also evidenced by profiles in both seasons (Fig. 3A–C). In spring the weakly mixed water column at Sta. CA18 (surface mixed-layer depth, ML$_D$ <4 m, 0.01 kg m^{-3} difference criterion) resulted in a swift decline of [CO] with depth within the upper 20 m, whereas stronger surface mixing at Sta. 303 (ML$_D$: 12–25 m) led to much less [CO] gradients in the upper 15 m. In autumn [CO] rapidly decreased with depth in the upper 15 and 10 m at Sta. 718 and CA6, while its distribution was much more uniform at Sta. CA12 and in the top 20 m at Sta. CA16. These distributions reflected the surface mixed-layer depths: shallow at Sta. CA6 (<1 m) and 718 (4 m), and deeper at Sta. CA12 (9 m) and CA16 (20 m). Biologically, a great variety of Chl *a* fluorescence profiles was encountered, but they exhibited no systematic relationship to CO profiles.

Water-column CO burdens from 0 m to 50 m, Σ^{50}CO (Fig. 4), were obtained by trapezoidal integration after
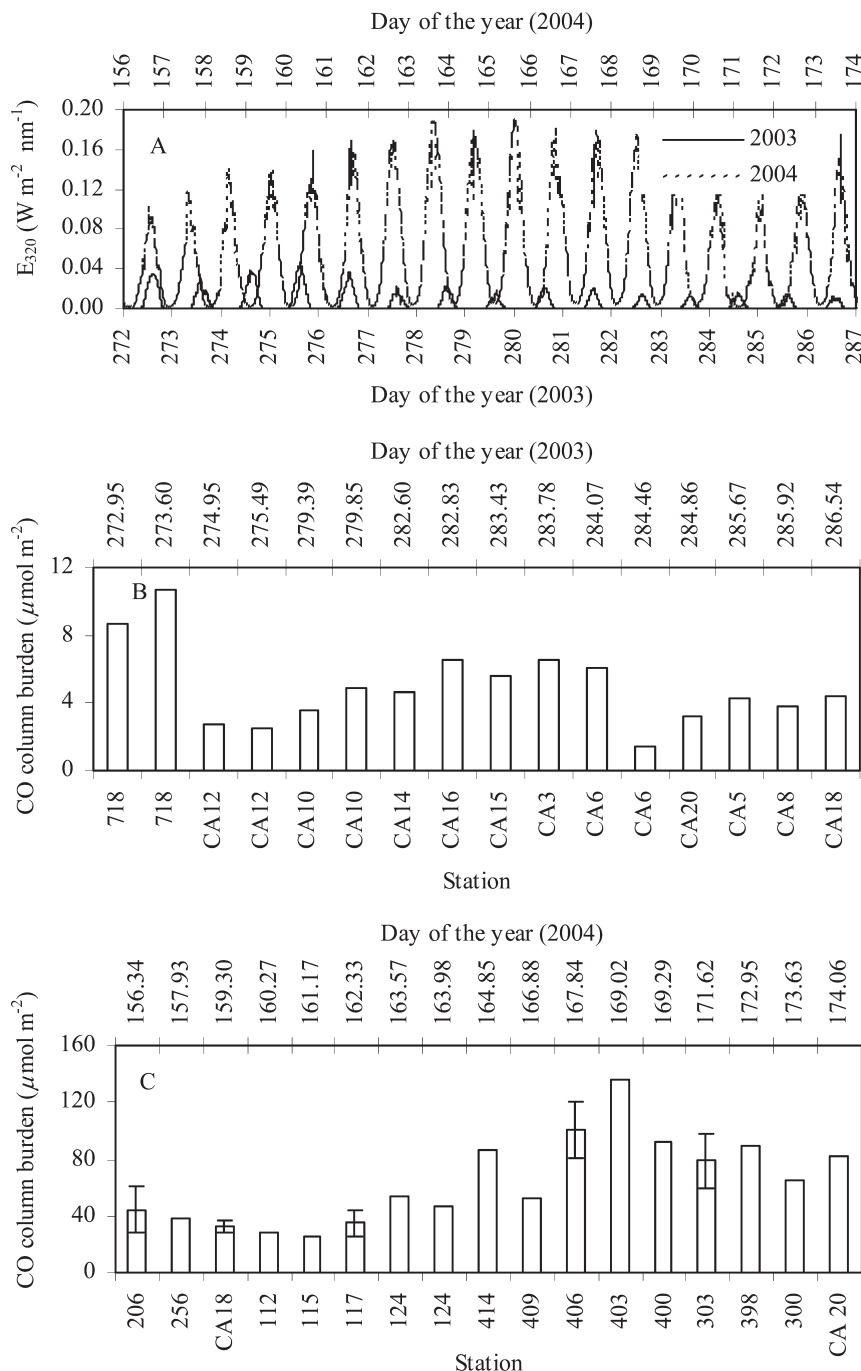
Fig. 4. (A) Temporal distributions of cosine-corrected surface irradiance at 320 nm (E_{320}), and (B) CO column burdens (0–50 m) in autumn, and (C) CO column burdens (0–50 m) in spring. Profile times (decimal year day) and column burdens were averaged for time-course stations in spring. Error bars are one standard deviation.

averaging duplicate subsamples. The mean $\Sigma^{50}CO$ in autumn in the entire study area was only slightly higher than that in the AG (Table 3), indicative of small regional variations in mean $\Sigma^{50}CO$. The maximum $\Sigma^{50}CO$ in autumn occurred at Sta. 718 (9.71 $\mu mol\ m^{-2}$) near the Mackenzie River estuary while the minimum occurred at the largely ice-covered Sta. CA12 (2.59 $\mu mol\ m^{-2}$). $\Sigma^{50}CO$

at Sta. CA6 dropped from 6.04 $\mu mol\ m^{-2}$ to 1.45 $\mu mol\ m^{-2}$ in 9.5 h from early morning (01:38 LT) to near noontime (11:38 LT), the largest on-station variation in $\Sigma^{50}CO$ encountered in autumn. For comparison, variations in $\Sigma^{50}CO$ at Sta. 718, CA10 and CA12 were only 23%, 37%, and 11% over time intervals of 11.2–15.8 h. In the AG, $\Sigma^{50}CO$ in spring spanned a much larger range

and averaged ~16-fold higher than in autumn (Table 3). A direct interseasonal comparison is possible for Sta. CA18 and CA20, which exhibited 7.5- and 25.8-fold higher $\Sigma^{50}CO$ in spring. Also, the spring Sta. 403 and 409 were near the autumn Sta. CA3 and CA5 (Fig. 1); the former had 21.0- and 12.3-fold higher $\Sigma^{50}CO$ than the latter. These trends roughly parallel the large seasonal differences in insolation, for example at 320 nm (Fig. 4). Among the spring stations, the mean $\Sigma^{50}CO$ in the central gulf was only 41% of the mean $\Sigma^{50}CO$ in areas further south and north (Figs. 1, 4). At the time-course stations, $\Sigma^{50}CO$ values were: Sta. CA18 (32.8 ± 4.7) < Sta. 117 (34.7 ± 9.1) < Sta. 206 (44.4 ± 16.8) < Sta. 303 (78.9 ± 19.3) < Sta. 406 (100.2 ± 19.4; parentheses indicate $\Sigma^{50}CO$ in $\mu mol\ m^{-2}$). Note that this order differs from that for the parallel mean $[CO]_{surf}$. No diurnal variations in $\Sigma^{50}CO$ were observed.

CO photoproduction—Fitted parameters for Eq. 1 along with other related data are shown in Table 2, while Fig. 5 displays representative a_{cdom} and Φ_{co} spectra for the upstream limit of the Mackenzie River estuary (Sta. R4), the freshwater–saltwater transitional zone (Sta. R5a), the MS (Sta. 718), and the AG (Sta. 117). Φ_{co} decreased seaward in both the UV and visible regimes, the differences in Φ_{co} widening progressively with increasing wavelength, as observed in a previous study (Zhang et al. 2006). Note that the temperature dependence of Φ_{co} (Zhang et al. 2006) should have increased Φ_{co} values for the ARDEX samples (Sta. R4, R5a, R5d, and R9), since they were irradiated at higher temperatures than the others (Table 2). Because no temperature effects were measured, the $\bar{\Phi}_{co}$ values defined in Eq. 2 for the ARDEX samples were corrected to $-0.5°C$, with unknown uncertainties, using the $\bar{\Phi}_{co}$–T relationships for samples from the St. Lawrence River estuary (Zhang et al. 2006). Sta. E4 had the highest $\bar{\Phi}_{co}$ value, followed sequentially by Sta. R4, R5d, R5a, and R9. Stations in the AG (CA18, 117, 409, and 414) gave the lowest $\bar{\Phi}_{co}$ values with little variability (1.22 ± 0.04 × 10^{-6}, $n = 4$). This trend was linearly inverse to salinity, excepting only the $\bar{\Phi}_{co}$ at Sta. E4 (much higher than expected). However, when $\bar{\Phi}_{co}$ is plotted against a_{cdom} (shown for example at 330 and 412 nm; Fig. 6A) all the data, including $\bar{\Phi}_{co}$ at Sta. E4, show a linear increase in $\bar{\Phi}_{co}$ with rising a_{cdom} with a very high correlation coefficient.

The CO photoproduction rate at the surface (0 m), $P_{co,0}$ (mol CO $m^{-3}\ d^{-1}$), is expressed as

$$P_{co,0} = \int_{300}^{600} Q_{0-,\lambda}\ a_{cdom,\lambda}\ \Phi_{co,\lambda}d\lambda \qquad (3)$$

where $Q_{0-,\lambda}$ is the scalar photon flux just beneath the surface at wavelength λ (mol photons $m^{-2}\ d^{-1}\ nm^{-1}$). The scalar photon flux was estimated to be 1.3 times the downwelling photon flux (Gordon 1989). Assuming vertically homogenous optical properties and negligible backscattering of light to the atmosphere, the CO photoproduction rate in the photic zone, $P_{co,col}$ (mol CO $m^{-2}\ d^{-1}$),

is given by

$$P_{co,col} = \int_{300}^{600} Q_{d,0-,\lambda}\ \frac{a_{cdom,\lambda}}{a_{t,\lambda}}\ \Phi_{co,\lambda}d\lambda \qquad (4)$$

where $Q_{d,0-,\lambda}$ is the downwelling photon flux just beneath the surface and $a_{t,\lambda}$ is the total absorption coefficient (m^{-1}): the sum of the absorption coefficients of CDOM, particles, and seawater. Mean subregional $a_{cdom,\lambda}:a_{t,\lambda}$ ratios were obtained from A. Matsuoka (unpubl.) for autumn and from Bélanger et al. (2006) for spring. The $a_{cdom}:a_t$ ratios at 330 nm, for example, are 0.81 (autumn) on the MS and 0.89 (autumn) and 0.93 (spring) in the AG. Daily $Q_{d,0-,\lambda}$ values were calculated using a radiative transfer method based on satellite measurements of total atmospheric ozone column and cloud cover as detailed in Bélanger et al. (2006). In light of the linear relationship between Φ_{co} and a_{cdom}, we fitted $\Phi_{co,\lambda}$ to the equation, $\Phi_{co,\lambda} = \alpha_\lambda + \beta_\lambda \times a_{330}$, where a_{330} is the CDOM absorption coefficient at 330 nm, α_λ and β_λ the fitted parameters, resulting in R^2 values of 0.947–0.996 (mean: 0.988) in the range 300–600 nm (*see* Web Appendix 2: www.aslo.org/lo/toc/vol_54/issue_1/0234a2.pdf). We chose a_{330} because 330 nm was near the wavelength at which maximum CO photoproduction occurs at the surface, but similar correlations were found at other wavelengths (e.g., 412 nm). Mean $\Phi_{co,\lambda}$ values for autumn and spring for each subregion (MS and AG) were calculated from the corresponding mean a_{330} values. Cruise-mean $P_{co,0}$ and $P_{co,col}$ were then computed from Eqs. 3 and 4 using the mean $a_{cdom,\lambda}:a_{t,\lambda}$ ratio and $\Phi_{co,\lambda}$ and the daily $Q_{d,0-,\lambda}$, $Q_{0-,\lambda}$.

In autumn the mean $P_{co,0}$ on the MS was 3.2 times that in the AG (12.4 vs. 3.9 nmol $L^{-1}\ d^{-1}$, Table 3), due both to higher CDOM concentration (a_{330}: 1.77 vs. 0.62 m^{-1}) and higher Φ_{co} on the shelf. The mean $P_{co,col}$ was, however, only 27% higher on the shelf than in the gulf (3.8 $\mu mol\ m^{-2}\ d^{-1}$ vs. 3.0 $\mu mol\ m^{-2}\ d^{-1}$), due primarily to the difference in Φ_{co}. In spring $P_{co,0}$ and $P_{co,col}$ in the gulf were 29.6 nmol $L^{-1}\ d^{-1}$ and 45.8 $\mu mol\ m^{-2}\ d^{-1}$, 7.7 and 15.2 times those in autumn, largely reflecting the much higher insolation then (Table 3; Fig. 4). Using the cruise-mean ice-free water areas derived above, we estimated the cruise-mean daily rate of CO photoproduction to be 280.3 mol on the MS (autumn) and 256.2 mol (autumn) and 1748.6 mol (spring) in the AG. These values are 9–18, 6–12, and 2.5–5 times climatological air–sea CO fluxes in the corresponding subregions and seasons, and the ratios would be even larger if instantaneous CO fluxes (Table 3) were used.

Microbial CO consumption—Results from the autumn cruise were reported previously (Xie et al. 2005). In summary, microbial CO uptake in autumn always followed first-order kinetics at ambient seawater [CO], with a mean k_{bio} of 0.69 ± 0.33 d^{-1} for the study area and 0.49 ± 0.22 d^{-1} for the AG (Table 3). The largest k_{bio} values occurred in a semi-closed inlet at Sta. E2 (1.39 d^{-1}) and at Sta. E3 (1.1 d^{-1}) and 718 (0.94 d^{-1}) close to the Mackenzie River estuary, whereas the smallest k_{bio} values occurred at
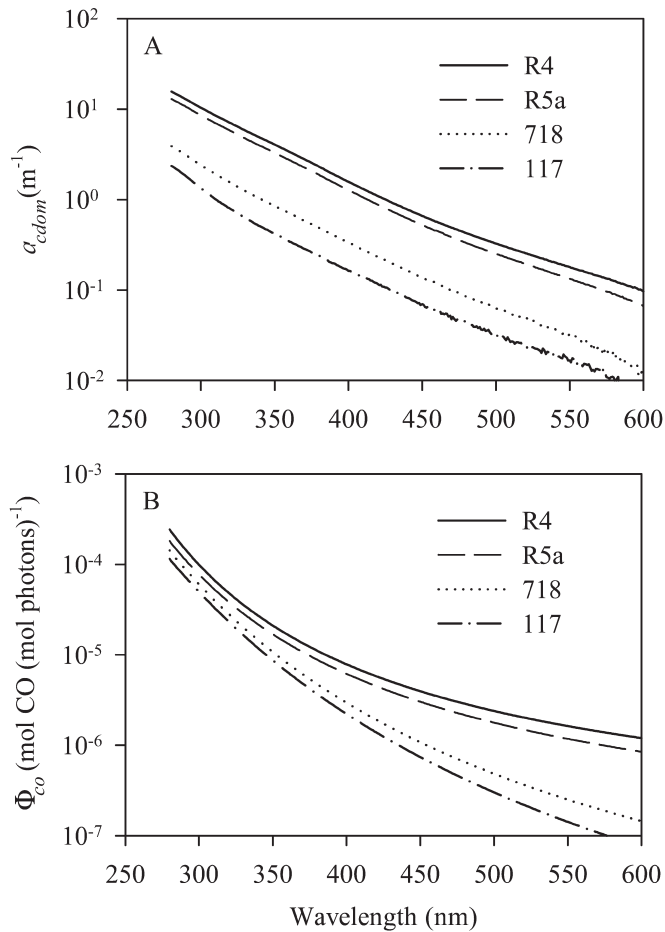
Fig. 5.   Representative spectra of (A) a_{cdom} and (B) CO AQY. Figure legends indicate station numbers.

Fig. 6.   Plots of $\overline{\Phi}_{co}$ as a function of (A) salinity (S) and CDOM absorption coefficients at 330 nm (a_{330}) and 412 nm (a_{412}) in this study and (B) a_{330} and a_{412} after including data from the St. Lawrence estuary (SLE; Zhang et al. 2006). Solid line is linear fit between $\overline{\Phi}_{co}$ and a_{330}, dashed line between $\overline{\Phi}_{co}$ and a_{412}, and dotted line between $\overline{\Phi}_{co}$ and salinity (excluding Sta. E4). Results of the fits are: (A) $\overline{\Phi}_{co} = 3.20 \times 10^{-7} \times a_{330} + 1.09 \times 10^{-6}$ ($R^2 = 0.981$, $n = 11$); $\overline{\Phi}_{co} = 1.36 \times 10^{-6} \times a_{412} + 1.12 \times 10^{-6}$ ($R^2 = 0.977$, $n = 11$), $\overline{\Phi}_{co} = -5.33 \times 10^{-8} \times S + 2.91 \times 10^{-6}$ ($R^2 = 0.938$, $n = 10$), and (B) $\overline{\Phi}_{co} = 3.24 \times 10^{-7} \times a_{330} + 1.12 \times 10^{-6}$ ($R^2 = 0.974$, $n = 16$); $\overline{\Phi}_{co} = 1.37 \times 10^{-6} \times a_{412} + 1.14 \times 10^{-6}$ ($R^2 = 0.976$, $n = 16$).

Sta. CA13 (0.46 d^{-1}), CA14 (0.26 d^{-1}), and Sta. CA16 (0.34 d^{-1}). Overall, k_{bio} increased linearly with [Ch a] ($R^2 = 0.944$, $n = 10$), indicating that [Ch a] was a useful surrogate for the activity of CO-consuming microbes in autumn. Wright–Hobbie kinetic studies of samples from Sta. E3 and CA4 gave V_{max} values of 4.10 (Sta. E3) and 1.75 (Sta. CA4) nmol L^{-1} d^{-1}, and K_m values of 1.5 (Sta. E3) and 0.8 (Sta. CA4) nmol L^{-1} CO.

Microbial CO uptake in spring was more complicated, varying from inhibition or saturation (zero-order) kinetics at elevated *ambient* [CO] to first-order kinetics at relatively low [CO] (Table 4). First-order uptake rate constants were 0.10–0.43 d^{-1}, averaging 0.23 d^{-1}, less than half of the autumn mean k_{bio} in the gulf and the two k_{bio} medians differed ~3-fold. A few vertical profiles of k_{bio} revealed slightly higher k_{bio} values at shallower depths (Table 4). No significant correlation between k_{bio} and [Chl a] was observed ($R^2 = 0.016$, $p = 0.76$), invalidating [Chl a] as an all-season indicator of k_{bio}. At two stations, CO uptake rate as a function of time and [CO] was studied in surface waters (Fig. 7) that exhibited in situ [CO] high enough to explore uptake kinetics at high substrate concentrations without adding any CO. The results indicate that CO uptake was saturated at ~3.5–6 nmol L^{-1} [CO] and
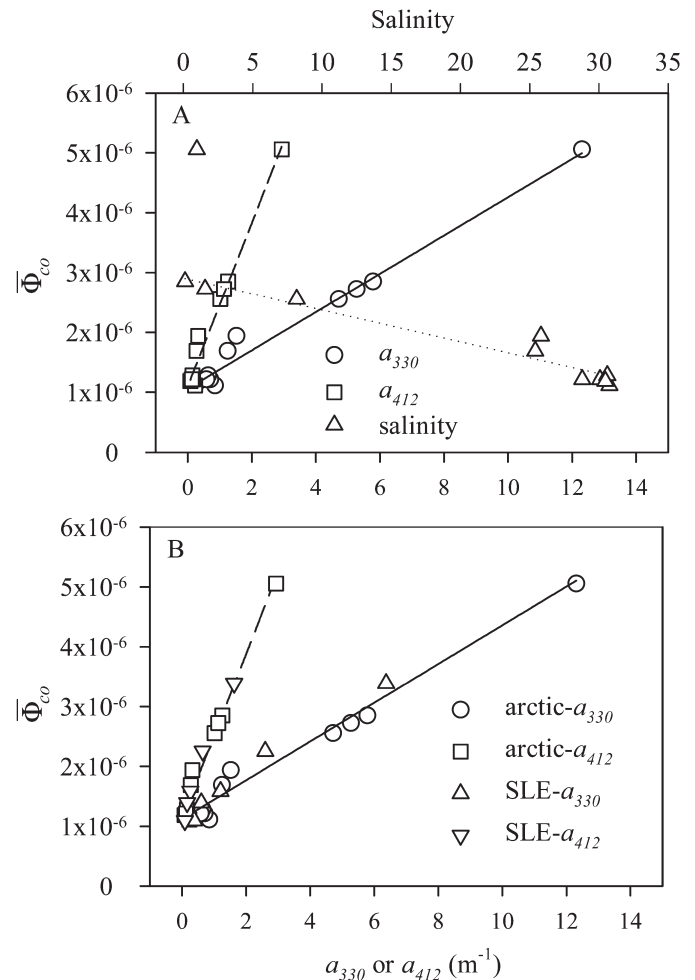
inhibited at ~7 nmol L^{-1} [CO] or higher. The plots of rate (V) against [CO] (excluding the inhibited points) show characteristic sigmoid shapes that differ from the Michaelis–Menten rectangular hyperbolas observed in autumn (fig. 6 in Xie et al. 2005). Note that the steepest part of the sigmoid curve shifts from the origin to positive [CO] values and the data are better fit by the Hill equation (Fig. 7; Table 5) than by the Michaelis–Menten equation. Best-fit Hill coefficients varied by a factor of three, V_{max} for Sta. 399 (3.4 nmol L^{-1} d^{-1}) was more than twice that for Sta. 117, while half-saturation [CO] values ($K_{0.5}$) were comparable. The kinetic data in spring thus suggest that microbial CO uptake oscillated among various kinetic states, likely in response to widely varying [CO]$_{surf}$ (Fig. 2; Table 3): first-

Table 4. Microbial CO consumption kinetics in spring. $[CO]_0$ is $[CO]$ at the start of incubation, which was close to in situ $[CO]$. N/A = Not applicable.

Sta.	Depth (m)	$[CO]_0$ (nmol L^{-1})	Kinetics	k_{bio} (d^{-1})
CA18	1.8	3.52	first-order	0.15
CA18	10	1.13	first-order	0.10
117	0	8.48	inhibition	N/A
117	5	2.42	first-order	0.43
117	15	0.34	first-order	0.38
206	2	2.23	first-order	0.16
206	10	0.86	first-order	0.12
206	20	0.22	first-order	0.14
399	2.4	7.90	inhibition	N/A
406	2.3	6.39	inhibition	N/A
406	10	2.96	first-order	0.34

order, mixed-order, zero-order, and inhibition. Vertically, at sufficiently high $[CO]_{surf}$, a succession of inhibition, zero-order, mixed order, and first-order kinetics may arise as $[CO]$ falls with depth (Fig. 3). For example, at in situ $[CO]$, uptake at Sta. 117 and 406 was inhibited at 0 m and 2.3 m, and first-order at 5 m and 10 m (Table 4). Zero-order and mixed-order kinetics likely occurred at 0–5 m at Sta. 117 and at 2.3–10 m at Sta. 406, since $[CO]$ within these layers decreased continuously with depth (data not shown).

Discussion

Factors controlling [CO] distributions—The most striking feature of $[CO]$ distribution in the upper oceans of mid- and low latitudes is its strong diurnal signature driven by periodic fluctuations in solar insolation and fast microbial CO removal (Johnson and Bates 1996; Zafiriou et al. 2008). This study reveals that pronounced diurnal $[CO]$ variations also occur, likely depending on season and location, in the much colder surface Arctic Ocean where microbial activities are thought to be considerably lower. A significant diurnal cycle, taken as 0.3 times the peak to trough difference divided by the daily mean, occurs at CO turnover times <36 h (Doney et al. 1995). According to this criterion, in autumn biological CO turnover times, τ_{bio} (k_{bio}^{-1}) alone were short enough to create discernible diurnal cycles at the surface at Sta. E2 (17.2 h), E3 (22.2 h), 718 (25.6 h), CA6 (32.2 h), and CA4 (35.7 h), but were too long to do so at Sta. CA5 (40.0 h), CA7 (41.7 h), CA10 (41.7 h), CA13 (52.6 h), CA16 (71.4 h), and CA14 (90.9 h). Note that all the former stations were in nearshore waters or within the Mackenzie River plume, while the latter stations were all in or near to the Canada Basin. Using the instantaneous fluxes and the Wanninkhof equation, the mean CO-loss rate constant in the surface mixed layer with respect to gas exchange, k_{ge}, was estimated to be 0.17 $\pm$ 0.19 d^{-1} ($n = 16$), corresponding to a mean gas exchange turnover time, τ_{ge}, of 141.4 h. Combining τ_{bio} and τ_{ge} leads to CO turnover times (τ_{co}) of <34 h at Sta. CA5 and CA10, implying diurnal variations there as well. Outgassing also substantially reduces the turnover times at Sta. CA13, CA14, and CA16 (38–56 h) but not to <36 h, and negligibly at mostly ice-covered Sta. CA7. In autumn the ratio of the means of τ_{ge} to τ_{bio} is 0.25, so that CO

outgassing was a sizable term, about 20% of total CO loss. In addition to microbial uptake and gas exchange, wind-induced mixing (dilution) could also have played a role in generating the diurnal $[CO]_{surf}$ signal in autumn, as suggested by the inverse linear relation between $[CO]_{surf}$
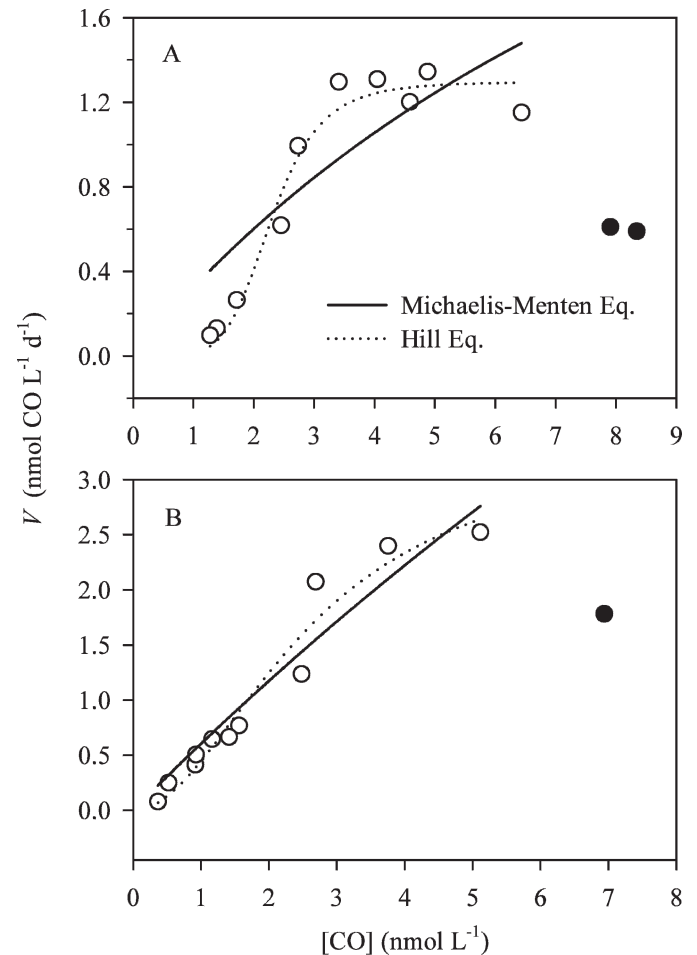

Fig. 7. Microbial CO uptake rate (V) vs. $[CO]$ for (A) Sta. 117 and (B) Sta. 399. Lines are the best fits to the Michaelis–Menten and Hill eqs. (*see* text and Table 5). Solid circles were excluded from the fitting.

Table 5.   Kinetic parameters of microbial CO uptake in waters from Sta. 117 (0 m) and 399 (2.4 m). The Hill equation is: $V = V_{max} \times [CO]^b / (K_{0.5}{}^b + [CO]^b)$ where V is the CO uptake rate, V_{max} the limiting uptake rate, $K_{0.5}$ the half-saturation [CO], and b the Hill coefficient. Standard error values are given in brackets. R^2_{adj} is adjusted for the degrees of freedom.

	Michaelis–Menten equation			Hill equation				
Sta.	V_{max} (nmol L^{-1} d^{-1})	K_m (nmol L^{-1})	R^2_{adj}	V_{max} (nmol L^{-1} d^{-1})	$K_{0.5}$ (nmol L^{-1})	b	R^2_{adj}	N
117	4.3(4.5)	12.4(17.2)	0.704	1.3(0.06)	2.3(0.1)	5.6(1.3)	0.956	10
399	20.8(31.0)	33.4(55.1)	0.926	3.4(0.8)	2.6(0.8)	2.0(0.5)	0.944	11

and wind speed (not shown) at Sta. E2 (k_{ge} there is only ~14% of k_{bio}).

In spring microbial CO uptake, as stated previously, oscillated among various kinetics, depending on [CO] as a function of time and depth. Taking first-order rate constants, k_{bio}, of 0.10–0.43 d^{-1} (mean: 0.23 d^{-1}) as upper limits gave τ_{bio} values of 55.8–240 h (mean: 104 h), far longer than the <36-h limit for significant diurnal signals. The mean k_{ge} in the surface mixed layer was assessed to be 0.20 ± 0.07 d^{-1} (range: 0.10–0.27 d^{-1}), yielding a mean τ_{ge} of 120 h (range: 88.9–240 h). Biology and outgassing then combined to yield an overall mean τ_{co} of 55.7 h. with the shortest τ_{co} value being 34.4 h. Diurnal cycles were, therefore, neither expected nor observed. Similar spring τ_{bio} and τ_{ge} values in the AG indicate that gas exchange, though usually a minor CO loss term at mid- and low latitudes (Zafiriou et al. 2003, 2008), can compare to biological processes as controls on CO turnover in cold waters.

Since abiotic, dark production of CO was minor in Arctic seawater (Xie et al. 2005), the steady-state CO column burden can be estimated as $P_{co,col} \times \tau_{co}$, giving mean values of 4.0 µmol m^{-2} in autumn and 106.0 µmol m^{-2} in spring. The autumn value agrees reasonably well with the mean observed $\Sigma^{50}CO$ of 4.9 µmol m^{-2}, implying that CO cycling was roughly at steady state. The spring estimate is 64% above the mean $\Sigma^{50}CO$ (64.8 µmol m^{-2}) but only 15% higher than the observed value late in the cruise (92.0 µmol m^{-2}, DOY 167–174). The spring CO-column burden was, therefore, far below its steady-state level in the beginning but approached this level by the season's end. However, the spring steady-state value is an underestimate, since first-order k_{bio} values were used to calculate τ_{co} while saturation and even inhibition kinetics were common then, so that the observed CO column burden even late in spring could still be well below the true steady-state level. In principle, then, low CO turnover rates in spring should lead to steady increases in $\Sigma^{50}CO$ with time, but although increases were observed the trend was not steady (Fig. 4). This discrepancy may result from horizontal advection of water masses, as evidenced by widely varying ML_D and concomitant current data (Y. Gratton pers. comm.). Horizontal transport of water masses with differing levels of CO (due to varying histories) may, thus, obscure the expected temporal trend. For example, advection of CO-depleted seawater from under sea ice into open water dilutes [CO], while influx of CO-enriched meltwater (Xie and Gosselin 2005) increases it.

However, the effects of using potentially biased $P_{co,col}$ and τ_{co} values may also play a role.

Extensive underway Pacific [CO]$_{surf}$ (~5 m) data (Bates et al. 1995) yielded regional and seasonal mean CO concentrations of 0.19–3.8 (median: 0.99) nmol L^{-1} for 15° latitude bands from 60°N to 75°S. The maximum, 3.8 nmol L^{-1}, observed in the Southern Ocean (60°–75°S) in austral summer, is close to the spring mean (4.72 nmol L^{-1}) in the Amundsen Gulf. Thus, maximum [CO]$_{surf}$ appears to occur consistently in polar oceans rather than at low and mid-latitudes ([CO]$_{surf}$: 0.26–1.88 nmol L^{-1}; 45°N–45°S). This effect may be due principally to slower microbial CO uptake rates in cold waters (Zafiriou et al. 2003; Xie et al. 2005). However, Bates et al. (1995)'s austral autumn [CO]$_{surf}$ in the 60°–75°S band, 0.99 nmol L^{-1}, is almost three times higher than the autumn mean (0.36 nmol L^{-1}) in the southeastern Beaufort Sea. Microbial CO consumption in the Arctic Ocean is likely facilitated by enrichment with terrestrial organic materials, in contrast to the Southern Ocean, which receives minimal terrigenous inputs (Zafiriou et al. 2003 vs. Xie et al. 2005).

CDOM photoreactivity—Samples from Sta. R4 (salinity: 0.13) and E4 (salinity: 0.97) were both nearly fresh but taken in different seasons: E4 in the high-flow springtime vs. R4 in the low-flow summertime. The much higher Φ_{co} value at Sta. E4 (Table 2, after T correction) thus indicates strong seasonal variability of Mackenzie River freshwater CDOM photoreactivity, which may result from CDOM experiencing longer light exposure and stronger microbial processing in summer. It could also be due to changes in the relative contribution of microbial CDOM vs. terrigenous river–derived CDOM. The latter likely originates mainly from soil-leached organic matter, with higher molecular weight, aromaticity, and photoreactivity (Zepp 2003). The $a_{365}:a_{250}$ ratio, an indicator of DOM molecular size (De Haan 1983; Lou and Xie 2006), for Sta. E4 (0.17) is 31% higher than for Sta. R4 (0.13), supporting the argument that CDOM in spring is "fresher" and/or more of terrestrial origin than in summer. Similarly, isotopic measurements of particulate organic matter and specific absorption comparisons of CDOM indicate that the river water during peak discharge in spring has a stronger terrigenous signal than during subsequent lower flow periods (Retamal et al. 2007).

The nearly linear downward trend of Φ_{co} with salinity (excluding Sta. E4 as discussed above; Fig. 6) likely results

from nearly conservative mixing of highly photoreactive terrestrial CDOM by less reactive marine CDOM. It could also be caused by matrix-induced structural changes in CDOM during estuarine mixing, since CDOM photoreactivity may decrease with increasing ionic strength (Minor et al. 2006) and increase with rising power of Hydrogen (pH) at pH >6 (K. Mopper_unpubl.). The slightly convex–upwards shape of the $\overline{\Phi}_{co}$ vs. salinity curve (Fig. 6A) suggests that such positive effects may outweigh the negative effects as Mackenzie River CDOM is transported seaward.

The strikingly linear relation between $\overline{\Phi}_{co}$ and absorption coefficients (Fig. 6A) proves the latter to be a useful indicator of CDOM reactivity with respect to CO photoproduction in the study area, as suggested previously by Stubbins (2001) and Zhang et al. (2006) for other coastal marine environments and applied by Stubbins (2006*b*). More interestingly, this relation also holds after including Zhang et al. (2006)'s St. Lawrence estuary data (Fig. 6B), and its generality is being further tested in our laboratory. As CDOM absorption coefficients may be retrieved by remote sensing (Johannessen et al. 2003; Bélanger et al. 2008; Fichot et al. 2008), the idea of space-based evaluation of marine CDOM photochemistry has been proposed recently (Siegel et al. 2002; Fichot 2004). Application of this idea is, however, somewhat hindered due to lack of information on regional and global variability of AQYs of CDOM photoproducts (C. Fichot and W. L. Miler unpubl.). The quantitative relationships between Φ_{co} and CDOM optical properties found in this and other studies, therefore, permit more accurate quantification of regional and global fluxes. Further studies should also be conducted to elucidate whether this proxy approach extends to other major CDOM photoprocesses, such as production of DIC, bio-labile organic carbon, and O_2 consumption. Note that the much smaller slope, as compared to the intercept, in the regression equation in Fig. 6 indicates a relatively small sensitivity of Φ_{co} to the absorption coefficient, so that Φ_{co} should encounter large decreases across freshwater–saltwater transitional zones, but that the variability of Φ_{co} should be limited in open oceans, where CDOM abundance is usually low, as confirmed by Zafiriou et al. (2003, 2008).

Implications of microbial CO uptake kinetics—As water temperature varied little between spring and autumn (Table 3), the halving of k_{bio} in spring suggests a substantial taxonomic shift or seasonal changes in the bacterial physiology influencing CO uptake. Bacterial measurements during CASES showed large changes in their nucleic acid and protein synthesis characteristics among seasons (Garneau et al. 2008), consistent with major shifts in community structure and physiology. More field surveys are required to clarify this issue. At ambient seawater [CO], microbial uptake has been observed to follow first- or mixed-order kinetics (Xie et al. 2005). The present study, to our knowledge, provides the first examples of saturation and inhibition kinetics for microbial CO uptake at in situ [CO] in natural waters, as well as Hill-type kinetics. However, interpreting Hill kinetics is not straightforward (Weiss 1997) and an alternative explanation of such curve shapes

based on energy limitations, which may be especially relevant in these Arctic waters, has been advanced (Button et al. 2004). Because of the prevalent low [CO] in the major ocean basins, it is believed that the potential of CO as a supplemental energy source to marine microbes is limited by [CO] (Moran and Miller 2007). Our results, however, demonstrate that in high-[CO] waters the high-affinity CO uptake enzyme system (i.e., low K_m) of the microbes also limits this potential. Future studies should elucidate why marine microbes have developed such a high-affinity, easily saturated and even substrate-inhibitable enzyme system, which apparently is not optimal in utilizing the already low abundance of CO as an energy source. Ecologically, saturation or inhibition kinetics leads to more CO being routed to the atmosphere, compared to first-order kinetics under otherwise identical conditions, and also points to important but complex roles of vertical mixing (dilution) in controlling CO loss in regions where saturation or inhibition kinetics occurs. Vertical mixing accelerates CO loss by enhancing gas exchange, diminishes it by dilution with deeper, low-[CO] waters, and further diminishes it indirectly by transforming saturation or inhibition kinetics into more efficient first-order kinetics.

Implications for DOC cycling—Using DIC AQY spectra determined on the same water samples as for Φ_{co} determination, Bélanger et al. (2006) estimated the mean annual DIC photoproduction from 1979 to 2003 to be 5.54 $\pm$ 1.54 $\times$ 10⁹ mol of carbon in the southeastern Beaufort Sea, a value equivalent to 10% of bacterial respiration rates, 8% of new primary production rates, and 5% of the 1.1×10^{11} mol of DOC discharged annually by the Mackenzie River. In 1998, when ice cover was historically low, DIC photoproduction could account for 9% of the riverine DOC flux, close to the value (11%) under an ice-free scenario. The station-to-station $\overline{\Phi}_{co}:\overline{\Phi}_{dic}$ ratio ($\overline{\Phi}_{dic}$ is the DIC AQY defined by Eq. 2) for the study area ranges from 8.3% to 13.8% and averages 11.1%. Including CO would, hence, raise the DOC loss via photomineralization by 11.1%, or 1.4×10^9 mol DOC yr⁻¹ under ice-free condition. The $\overline{\Phi}_{co}:\overline{\Phi}_{dic}$ ratio obtained in this study is also well above the similarly defined ratios observed in warmer waters (5–7%; Miller and Zepp 1995; D. J. Kieber pers. comm.), implying significant regional variability of this parameter. Caution therefore is needed in extrapolations of DOC photoremineralization rates derived using CO as a proxy from one region to another or to global scales.

References

BABIN, M., D. STRAMSKI, G. M. FERRARI, H. CLAUSTRE, A. BRICAUD, G. OBOLENSKY, AND N. HOEPFFNER. 2003. Variations in the light absorption coefficients of phytoplankton, nonalgal particles, and dissolved organic matter in coastal waters around Europe. J. Geophys. Res. **108:** 3211, doi:10.1029/2001JC000882.

BATES, T. S., K. C. KELLY, J. E. JOHNSON, AND R. H. GAMMON. 1995. Regional and seasonal-variations in the flux of oceanic carbon-monoxide to the atmosphere. J. Geophys. Res. **100:** 23093–23101.

Bélanger, S., M. Babin, and P. Larouche. 2008. An empirical ocean color algorithm for estimating the contribution of chromophoric dissolved organic matter to total light absorption in optically complex waters. J. Geophys. Res. **113:** C04027, doi:10.1029/2007JC004436.

———, H. Xie, N. Krotkov, P. Larouche, W. F. Vincent, and M. Babin. 2006. Photomineralization of terrigenous dissolved organic matter in Arctic coastal waters from 1979 to 2003: Interannual variability and implications of climate change. Global. Biogeochem. Cycles **20:** GB4005, doi:10.1029/2006GB002708.

Buiteveld, H., J. M. H. Hakvoort, and M. Donze. 1994. The optical properties of pure water, p. 174–183. *In* J. S. Jaffe [ed.], SPIE proceedings on ocean optics XII. The Society of Photo-Optical Instrumentation Engineers.

Button, D. K., B. Robertson, E. Gustafson, and X. Zhao. 2004. Experimental and theoretical bases of specific affinity, a cytoarchitecture-based formulation of nutrient collection proposed to supercede the Michaelis–Menten paradigm of microbial kinetics. Appl. Env. Microbiol. **70:** 5511–5521.

Carmack, E. C., and R. W. Macdonald. 2002. Oceanography of the Canadian shelf of the Beaufort Sea: A setting for marine life. Arctic **55:** 29–45.

Conrad, R., W. Seiler, G. Bunse, and H. Giehl. 1982. Carbon monoxide in seawater (Atlantic Ocean). J. Geophys. Res. **87:** 8839–8852.

De Haan, H. 1983. Use of ultraviolet spectroscopy, gel filtration, pyrolysis/mass spectrometry and numbers of benzoate metabolizing bacteria in the study of humification and degradation of aquatic organic matter, p. 165–182. *In* R. F. Christman and E. T. Gjessing [eds.], Aquatic and terrestrial humic materials. Ann Arbor Science.

Dittmar, T., and G. Kattner. 2003. The biogeochemistry of the river and shelf ecosystem of the Arctic Ocean: A review. Mar. Chem. **83:** 103–120.

Doherty, K. W., C. D. Taylor, and O. C. Zafiriou. 2003. Design of a multi-purpose titanium bottle for uncontaminated sampling of carbon monoxide and potentially of other analytes. Deep-Sea Res. I **50:** 449–455.

Doney, S. C., R. G. Najjar, and S. Stewart. 1995. Photochemistry, mixing and diurnal cycles in the upper ocean. J. Geophys. Res. **53:** 341–369.

Fichot, C. G. 2004. Marine photochemistry from space. M.S. thesis. Dalhousie Univ.

———, S. Sathyendranath, and W. L. Miller. 2008. SeaUV and SeaUVC: Algorithms for the retrieval of UV/Visible diffuse attenuation coefficients from ocean color. Remote Sens. Environ. **112:** 1584–1602.

Fioletov, V. E., and others. 2004. UV index climatology over the United States and Canada from ground-based and satellite estimates. J. Geophys. Res. **109:** D22308, doi:10.1029/2004JD004820.

Flato, G. M., G. J. Boer, W. G. Lee, N. A. McFarlane, D. Ramsden, M. C. Reader, and A. J. Weaver. 2000. The Canadian centre for climate modelling and analysis global coupled model and its climate. Clim. Dynam. **16:** 451–467.

Frey, K. E., and L. C. Smith. 2005. Amplified carbon release from vast West Siberian peatlands by 2100. Geophys. Res. Lett. **32:** L09401, doi:10.1029/2004GL022025.

Galand, P. E., C. Lovejoy, J. Pouliot, M.-E. Garneau, and W. F. Vincent. 2008. Microbial community diversity and heterotrophic production in a coastal Arctic ecosystem: A stamukhi lake and its source waters. Limnol. Oceanogr. **53:** 813–823.

Garneau, M.-È., S. Roy, C. Lovejoy, Y. Gratton, and W. F. Vincent. 2008. Seasonal dynamics of bacterial biomass and production on the Arctic shelf: Franklin Bay, western Canadian Arctic. J. Geophys. Res. **113:** C07S91, doi:10.1029/2007JC004281.

Gordon, H. R. 1989. Can the Lambert-beer law be applied to the diffuse attenuation coefficient of ocean water. Limnol. Oceanogr. **34:** 1389–1409.

Gueymard, C. A. 2001. Parameterized transmittance model for direct beam and circumsolar spectral irradiance. Sol. Energy **71:** 325–346.

Hu, C. M., F. E. Muller-Karger, and R. G. Zepp. 2002. Absorbance, absorption coefficient, and apparent quantum yield: A comment on common ambiguity in the use of these optical concepts. Limnol. Oceanogr. **47:** 1261–1267.

Johannessen, S. C., and W. L. Miller. 2001. Quantum yield for the photochemical production of dissolved inorganic carbon in seawater. Mar. Chem. **76:** 271–283.

———, ———, and J. J. Cullen. 2003. Calculation of UV attenuation and colored dissolved organic matter absorption spectra from measurements of ocean color. J. Geophys. Res. **108:** 3301, doi:10.1029/2000JC000514.

Johnson, J. E., and T. S. Bates. 1996. Sources and sinks of carbon monoxide in the mixed layer of the tropical South Pacific Ocean. Global Biogeochem. Cycles. **10:** 347–359.

King, G. M., and C. F. Weber. 2007. Distribution, diversity and ecology of aerobic CO-oxidizing bacteria. Nat. Rev. Microbiol. **5:** 107–118.

Linnenbom, V. J., J. W. Swinnerton, and R. A. Lamontagne. 1973. The ocean as a source for atmospheric carbon monoxide. J. Geophys. Res. **78:** 5333–5340.

Liss, P. S., and L. Merlivat. 1986. Air–sea exchange rates: Introduction and synthesis, p. 113–127. *In* P. Buat-Menard [ed.], The role of air–sea exchange in geochemical cycling. D. Reidel.

Lou, T., and H. Xie. 2006. Photochemical alteration of the molecular weight of dissolved organic matter. Chemosphere **65:** 2333–2342.

Miller, W. L., M. A. Moran, W. M. Sheldon, R. G. Zepp, and S. Opsahl. 2002. Determination of apparent quantum yield spectra for the formation of biologically labile photoproducts. Limnol. Oceanogr. **47:** 343–352.

———, and R. G. Zepp. 1995. Photochemical production of dissolved inorganic carbon from terrestrial organic-matter— significance to the oceanic organic carbon cycle. Geophys. Res. Lett. **22:** 417–420.

Minor, E. C., J. Pothen, B. J. Dalzell, H. Abdulla, and K. Mopper. 2006. Effects of salinity changes on the photodegradation and ultraviolet-visible absorbance of terrestrial dissolved organic matter. Limnol. Oceanogr. **51:** 2181–2186.

Mopper, K., and D. J. Kieber. 2000. Marine photochemistry and its impact on carbon cycling, p. 101–129. *In* S. de Mora, S. Demers and M. Vernet [eds.], The effects of UV radiation in the marine environment. Cambridge Univ. Press.

Moran, M. A., and others. 2004. Genome sequence of *Silicibacter pomeroyi* reveals adaptations to the marine environment. Nature **432:** 910–913.

———, and W. L. Miller. 2007. Resourceful heterotrophs make the most of light in the coastal ocean. Nat. Rev. Microbiol. **5:** 792–800.

Novelli, P. C., K. A. Masarie, and P. M. Lang. 1998. Distributions and recent changes of carbon monoxide in the lower troposphere. J. Geophys. Res. **103:** 19015–19033.

Opsahl, S., and R. Benner. 1998. Photochemical reactivity of dissolved lignin in river and ocean waters. Limnol. Oceanogr. **43:** 1297–1304.

———, ———, AND R. M. W. AMON. 1999. Major flux of terrigenous dissolved organic matter through the Arctic Ocean. Limnol. Oceanogr. **44:** 2017–2023.

POPE, R. M., AND E. S. FRY. 1997. Absorption spectrum (380–700 nm) of pure water .2. Integrating cavity measurements. Appl. Optics **36:** 8710–8723.

RETAMAL, L., W. F. VINCENT, C. MARTINEAU, AND C. L. OSBURN. 2007. Comparison of the optical properties of dissolved organic matter in two river-influenced coastal regions of the Canadian Arctic. Estuar. Coast. Shelf Sci. **72:** 261–272.

SIEGEL, D. A., S. MARITORENA, N. B. NELSON, D. A. HANSELL, AND M. LORENZI-KAYSER. 2002. Global distribution and dynamics of colored dissolved and detrital organic materials. J. Geophys. Res. **107:** 3228, doi:10.1029/2001JC000965.

SMITH, S., M. A. BOURASSA, AND R. J. SHARP. 1999. Establishing more truth in true winds. J. Atmos. Ocean. Technol. **16:** 939–952.

STUBBINS, A. 2001. Aspects of aquatic CO photoproduction from CDOM. Ph.D. thesis. Univ. Newcastle-upon-Tyne.

———, G. UHER, V. KITIDIS, C. S. LAW, R. C. UPSTILL-GODDARD, AND E. M. S. WOODWARD. 2006a. The open-ocean source of atmospheric carbon monoxide. Deep-Sea Res. II **53:** 1685–1694.

———, ———, C. S. LAW, K. MOPPER, C. ROBINSON, AND R. C. UPSTILL-GODDARD. 2006b. Open-ocean carbon monoxide photoproduction. Deep-Sea Res. II **53:** 1695–1705.

SWINNERTON, J. W., V. J. LINNENBOM, AND R. A. LAMONTAGNE. 1970. The ocean: A natural source of carbon monoxide. Science **167:** 984–986.

THOMPSON, A. M. 1992. The oxidizing capacity of the Earth's atmosphere—probable past and future changes. Science **256:** 1157–1165.

TOLLI, J. D., S. M. SIEVERT, AND C. D. TAYLOR. 2006. Unexpected diversity of bacteria capable of carbon monoxide oxidation in a coastal marine environment, and contribution of the *Roseobacter*-associated clade to total CO oxidation. Appl. Environ. Microbiol. **72:** 1966–1973.

———, AND C. D. TAYLOR. 2005. Biological CO oxidation in the Sargasso Sea and in Vineyard Sound, Massachusetts. Limnol. Oceanogr. **50:** 1205–1212.

WANNINKHOF, R. 1992. Relationship between wind speed and gas exchange over the ocean. J. Geophys. Res. **97:** 7373–7382.

WEISS, J. N. 1997. The Hill equation revisited: Uses and misuses. FASEB J. **11:** 835–841.

WIESENBURG, D. A., AND J. N. L. GUINASSO. 1979. Equilibrium solubilities of methane, carbon monoxide, and hydrogen in water and seawater. J. Chem. Eng. Data **24:** 356–360.

XIE, H., S. S. ANDREWS, W. R. MARTIN, J. MILLER, L. ZIOLKOWSKI, C. D. TAYLOR, AND O. C. ZAFIRIOU. 2002. Validated methods for sampling and headspace analysis of carbon monoxide in seawater. Mar. Chem. **77:** 93–108.

———, AND M. GOSSELIN. 2005. Photoproduction of carbon monoxide in first-year sea ice in Franklin Bay, southeastern Beaufort Sea. Geophys. Res. Lett. **32:** L12606, doi:10.1029/2005GL022803.

———, O. C. ZAFIRIOU, T. P. UMILE, AND D. J. KIEBER. 2005. Biological consumption of carbon monoxide in Delaware Bay, NW Atlantic and Beaufort Sea. Mar. Ecol. Prog. Ser. **290:** 1–14.

ZAFIRIOU, O. C., S. S. ANDREWS, AND W. WANG. 2003. Concordant estimates of oceanic carbon monoxide source and sink processes in the Pacific yield a balanced global "blue-water" CO budget. Glob. Biogeochem. Cycles **17:** 1015, doi:10.1029/2001GB001638.

———, H. XIE, N. B. NELSON, R. JAJJAR, AND W. WANG. 2008. Diel carbon monoxide cycling in the upper Sargasso Sea near Bermuda at the onset of spring and in mid-summer. Limnol. Oceanogr. **53:** 835–850.

ZEPP, R. G. 2003. Solar UVR and aquatic carbon, nitrogen, sulfur and metals cycles, p. 137–184. *In* E. W. Helbling and H. Zagarese [eds.], UV effects in aquatic organisms and ecosystems. The Royal Society of Chemistry.

ZHANG, Y., H. XIE, AND G. H. CHEN. 2006. Factors affecting the efficiency of carbon monoxide photoproduction in the St. Lawrence estuarine system (Canada). Environ. Sci. Technol. **40:** 7771–7777.

ZIOLKOWSKI, L. A., AND W. L. MILLER. 2007. Variability of the apparent quantum efficiency of CO photoproduction in the Gulf of Maine and Northwest Atlantic. Mar. Chem. **105:** 258–270.